ChemComm
Chemical Communications

Accepted Manuscript

This article can be cited before page numbers have been issued, to do this please use: A. Usha Vijayakumar, M. Shanmugasundaram, V. Thazhe Veetil and D. Zitoun, *Chem. Commun.*, 2026, DOI: 10.1039/D6CC01926A.

ROYAL SOCIETY OF CHEMISTRY

rsc.li/chemcomm

ChemComm

View Article Online
DOI: 10.1039/D6CC01926A

COMMUNICATION

Ni_4N Interspersed Ru for Enhanced Hydrogen Oxidation Reaction in Alkaline Medium

Anagha Usha Vijayakumar[#], Manoj Shanmugasundaram[#], Vineesh Thazhe Veettil and David Zitoun*

Received 00th January 20xx,
Accepted 00th January 20xx

DOI: 10.1039/x0xx00000x

We report on a Ru-Ni_4N/C heterostructured catalyst, prepared by selective Ni nitridation during RuNi alloy annealing in NH_3. It outperforms Pt/C, RuNi alloy and Ru/C in alkaline hydrogen oxidation reaction (HOR), with specific activity of 0.4 mA cm^{-2} at 0.1 V vs. RHE twice above Ru/C, due to optimized H binding energy and enhanced water adsorption via Ni alloying and heterostructure formation.

Proton exchange membrane fuel cells (PEMFC) and anion exchange membrane fuel cells (AEMFC), operating in acid and alkaline media respectively are the focal points of green energy production. The two vital reactions underpinning these fuel cells are the oxygen reduction reaction (ORR) and the hydrogen oxidation reaction (HOR).[1,2] A hindrance to the commercialization of fuel cells is the high loading of precious metal-based catalysts (Pt based materials).[3] While in PEMFCs, an ultra-low loading of Pt renders remarkable HOR performance, high Pt loadings are required to compensate the sluggish ORR kinetics. The AEMFCs overtop PEMFCs by operating in less corrosive environments and enabling the use of non-Pt based catalysts for ORR. The ORR activity of non-precious metal catalysts is on par with the platinum group metals (PGM).[4] However, there emerges a new challenge: the HOR kinetics on Pt surfaces is two orders of magnitude lower than in acid, necessitating a higher loading.[5] This sluggish kinetics necessitates considerable research dedicated to the development of alternative HOR catalysts for alkaline fuel cells.

Alkaline medium allows the usage of non-precious metals as electrocatalysts. However, tailoring non-precious metal centres, which satisfies the energy demands, is still a big challenge on the anode side. H_2 adsorbs and dissociates as hydrides on most transition metal surfaces with heats of chemisorption between 60 and 120 kJ mol^{-1}.[6] Among all those transition metals, Ni-based materials, as a non-precious metal centre, can activate the slow reactions of hydrogen, i.e., HER and HOR.[7–9] Nickel nitrides and carbides have been reported as good HER electrocatalysts, and HOR electrocatalysts provided that their stability upon anodic polarization (potential breakdown) can be solved.[10–13] Indeed, the surface oxidation of nickel-based phase (including nitrides and carbides) in alkaline medium inhibits the HOR activity. Therefore, the durability of these earth-abundant HOR catalysts is thermodynamically questionable.

On the other hand, recent studies on HOR catalyst suggest that an improvement in activity and stability can be achieved by the addition of foreign metal atoms either segregated on the surface of PGMs or in the form of bimetallic alloys.[5,14-17] Consequently, the alloying or partial coating of low-cost transition metals with a small amount of PGMs should be the better way for high activity, low cost and durable HOR electrocatalysts for AEMFCs.[5,18–22] With the exception of Pt, the electrocatalytic activity of Ru is one of the highest among the pure metals for HOR. Ru is oxophilic and has moderate hydrogen adsorption free energy. The electrocatalytic activities of pure Ru is still lower than that of Pt, which prevents it from being used directly in fuel cells. In recent years great efforts have been dedicated to improving the activity of Ru by surface modification and alloying.[23–26] Alloying of Ru with other transition metals (Ni, Co, Fe and Mn) has been recognized as an effective strategy to enhance the electrocatalytic activity and to reduce the cost.[14] Bimetallic Ru systems have been extensively explored for HOR in the past few years. Among them alloying Ru with Ni has great potential to improve the kinetics of HOR/HER.[27–32] DFT studies on the alloying effect of nickel has demonstrated that it reduces the hydrogen binding energy and energy barrier of water formation.[5,33] The oxophilicity of Ni benefits the HOR activity of Ru. In addition to alloying, surface structure modifications such as heterostructuring and interface engineering have shown success in fine tuning the hydrogen binding energy and water adsorption. Yanrong *et.al*,[28] demonstrated that RuNi alloy after annealing in air exhibit improved catalytic

Department of Chemistry, Bar-Ilan Institute of Nanotechnology and Advanced Materials (BINA), Israel National Institute for Energy Storage (INIES), Bar-Ilan University, Ramat Gan, 5290002, Israel

*Corresponding Author: E-mail address: david.zitoun@biu.ac.il

[#] Equal contribution

performance owing to the formation of surface oxides. The surface nickel oxides play an active role in enhancing water adsorption, while the metallic nickel mitigates the excessively strong hydrogen binding energy. Interface chemistry and heterostructuring were effectively manipulated to deliver a better HOR performance for Pt/NiO by virtue of a decreased HBE after annealing. Contrary to oxides which are either semiconducting or insulating, metal nitrides which are intrinsically metallic are more promising. In this context, interface engineering of metals with Ni_3N enabled a close to ideal ΔG_{H^*} value. [11,31,34]

In this present study, we synthesized Ru-Ni alloys on Vulcan carbon by a wet impregnation followed by thermal reduction method. Further annealing under ammonia yielded Ru-Ni_4N/C dealloyed heterostructures. Ru-Ni_4N/C heterostructures showed better performance toward HOR in comparison to their alloy counterparts and even compared to Pt/C. This study opens a new platform for the synthesis of highly active HOR catalysts by interface engineering.

Figure 1(A) displays TEM images of synthesized catalysts (1. RuNi-7030, 2. RuNi-8515, 3. RuNi$_4$N-7030 and 4. RuNi$_4$N-8515), revealing uniformly dispersed nanoparticles on the carbon support with an average size of ~2.2 nm. Remarkable, the particle size further decreases after annealing at 350°C in NH_3, which can be attributed to mild surface etching by ammonia and the formation of thermodynamically stable nickel nitride phases that induce lattice contraction and structural rearrangement. Figure 1B shows High-angle annular dark field- scanning transmission electron microscopy (HAADF-STEM), elemental maps and line-scan profile for a representative RuNi$_4$N-8515 nanoparticle, evidencing a homogeneous distribution of Ru and Ni across the particle. The overlapped elemental maps confirm homogeneous mixing of two metals, while similarly mapping for RuNi$_4$N-7030/C (Figure S1) demonstrates similarly uniform Ru and Ni dispersion. Together with the presence of N signals in both the nanoparticles and carbon regions, these data indicate that NH_3 treatment leads to nitrogen incorporation into the metal phase as well as N-doping of the carbon support. The energy dispersive X-ray spectroscopy (EDX) line profile in Figure 1B confirms the coexistence of Ru and Ni within individual nanoparticles. Bulk elemental compositions derived from high resolution scanning electron microscopy (HRSEM)-EDX (Table S1) agree well with the nominal feed ratios, further supporting successful synthesis of composition-tuned RuNi and RuNiN catalysts. Additional TEM images of all catalysts (Figure S2) consistently show a uniform nanoparticle distribution over the carbon matrix, providing a high density of accessible active sites for HOR. The ammonia treatment preserves the high dispersion and small particle size of the samples (Figure S3).

The crystal structure of catalysts was examined by powder X-ray diffraction (XRD, Figure 2). In contrast to Ru/C, RuNi-7030/C and RuNi-8515/C samples do not show distinct diffraction peaks, which is likely due to their relatively low metal loadings and the ultrasmall particle size.

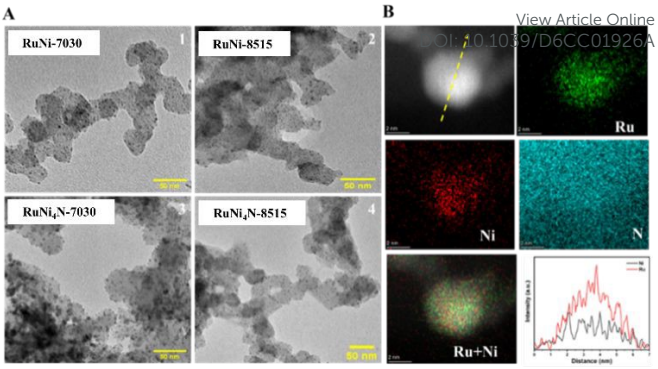

Figure 1. Electron microscopy images. A (1) Transmission electron microscopy (TEM) images of the RuNi-7030, A (2) TEM images of the RuNi-8515, A (3) TEM images of the RuNi$_4$N-7030 and A (4) TEM images of the RuNi$_4$N-8515. B. High angle annular dark field-scanning transmission electron microscopy elemental mapping of RuNi$_4$N-8515and Line profile mapping of Ru and Ni (yellow dotted line) nanoparticle.

After NH_3 treatment at 350°C, Ni reacts with nitrogen to form Ni_4N, and diffraction peaks characteristic of the RuNi alloy and Ni_4N phase emerge for RuNi-7030/C (denoted RuNi$_4$N-7030/C, Figure 2b). By comparison, no clear diffraction peaks are observed for NH3-treated RuNi-8515/C (RuNi$_4$N-8515/C), consistent with its lower Ni content. Furthermore, no additional reflections assignable to Ru nitrides are detected, indicating that N incorporation into the Ru lattice (RuN formation) does not occur under these conditions.

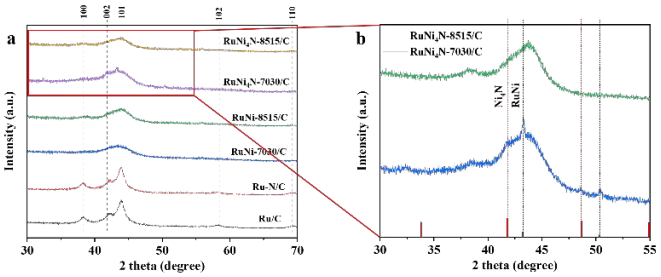

Figure 2. (a). XRD pattern of Ru/C, Ru-N/C, RuNi-7030/C, RuNi-8515/C, RuNi$_4$N-7030/C and RuNi$_4$N-8515/C. (b) Enlarged XRD patterns of RuNi$_4$N-7030, RuNi$_4$N-8515, highlighting RuNi and Ni_4N-related diffraction features.

X-ray photoelectron spectroscopy (XPS) was employed to probe the surface composition and chemical states of RuNi$_4$□/C catalysts, including RuNi-7030/C, RuNi-8515/C, and their nitride analogues. High-resolution XPS spectra of RuNi$_4$N-8515and RuNi$_4$N-7030 are displayed in Figure 3A and 3B, respectively. In the Ru 3p spectrum of Ru/C, a peak at 462.3 eV corresponds to metallic Ru $3p_{3/2}$ (Figure S4) but appears at a higher binding energy than bulk Ru (461.4 eV), reflecting strong metal-support interactions with carbon. The higher electronegativity of carbon (2.55) relative to Ru (2.2) withdraws electron density from Ru, leading to an upshift in biding energy. Additional peaks at 466.0

eV and 470.8 eV are assigned to surface-oxidized Ru^{4+} species and the satellite peak, respectively.

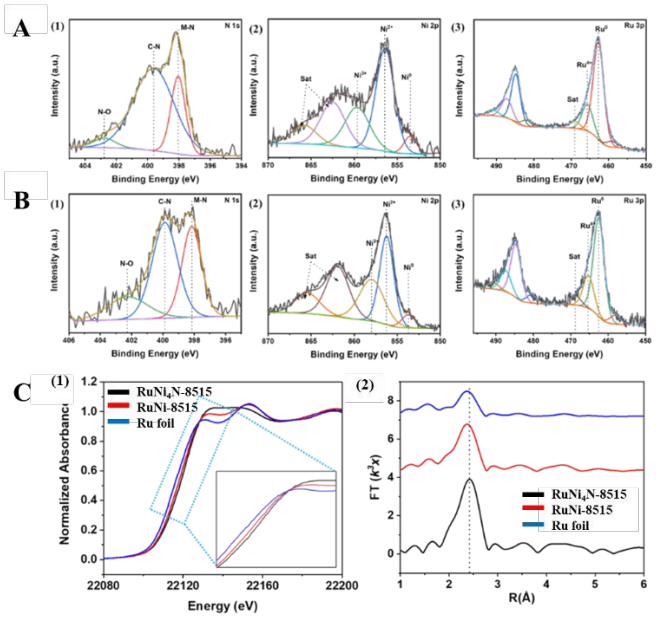

Figure 3. Surface and local structural characterization. (A) High- resolution XPS spectra of $RuNi_4N$-8515/C. (1) N1s, (2) Ni 2p, (3) Ru 3p. B. High-resolution XPS spectra of $RuNi_4N$-7030/C: (1) N1s, (2) Ni 2p, and (3) Ru 3p. C. Ru K-edge XAS: (1) normalized XANES spectra and (2) magnitude of Fourier-transformed EXAFS for RuNi-8515/C, $RuNi_4N$-8515/C, and Ru foil.

For, RuNi-7030/C and RuNi-8515/C, the Ni 2p spectra exhibit metallic Ni $2p_{3/2}$ peaks at 853.8 and 853.7 respectively (Figure S5 and S6), while the corresponding Ru 3p metallic peaks are further shifted to 462.4 and 462.5 eV, evidencing electronic perturbation of Ru induced by Ni incorporation. [27,30-31] The N 1s spectra (Figure 3A1, 3B1) confirm nitrogen incorporation on both metal and carbon matrix, as indicated by M–N and C–N contributions. In the nitride samples $RuNi_4N$-7030 and $RuNi_4N$-8515 (Figure 3A2, 3B2), Ni 2p peaks shift to lower binding energy relative to their non-nitride counterparts, whereas Ru 3p peaks at 462.6 eV and 462.8 eV (Figure 3A3, 3B3) shift to higher binding energy. These opposites shifts point to substantial reorganization of the Ru-Ni electronic structure upon N-doping.

To further elucidate the electronic and geometric structure of Ru, Ru K-edge X-ray absorption spectroscopy (XAS) was carried out for RuNi-8515, $RuNi_4N$-8515, and Ru foil. The normalized X-ray absorption near-edge structure (XANES) spectra (Figure 3C1) display an increased white-line intensity and a positive absorption edge shift for the RuNi alloy compared with Ru foil. Fourier-transformed (FT) extended X-ray absorption fine structure (EXAFS) spectra in R-space (Figure 3C2) show a main peak at 2.42 Å for Ru foil, whereas RuNi-8515/C and $RuNi_4N$-8515/C exhibit a peak at ~2.36 Å assignable to Ru–Ni coordination.[29,31] The Ru K-edge FT-EXAFS spectra of $RuNi_4N$-8515/C corresponds to a statistical alloy. Upon quantitative fitting, this feature is assigned to Ru–Ni with a coordination number of 6 (CN = 6), an amplitude reduction factor $S_0^2 = 0.938$, a Debye–Waller factor $\sigma^2 = 0.00402$ Å², and a phase-corrected bond distance R = 2.67 Å. The small difference of 0.3 Å between the FT peak position and the fitted distance arises from the EXAFS phase shift, within the typical range reported for transition-metal K-edge EXAFS (Figure S9). The relatively small σ^2 value reflects a swell-ordered first coordination shell, suggesting a uniform local Ru–Ni environment.

Cyclic voltammetry was conducted in N_2-saturated 0.1M KOH to probe the electrochemical surface features of the $RuNi_4N$/C catalysts. As shown in Figure 4a, Pt/C displays the characteristic hydrogen underpotential deposition (H-UPD) region of Pt, with distinct peaks associated with different planes, together with a well-defined double layer and surface redox features. The first H-UPD peak of Pt/C appears at 0.28 V vs RHE, whereas Ru/C shows a pronounced H-UPD peak at 0.14 V vs RHE, and RuNi-8515/C and $RuNi_4N$-8515/C shifts this feature further to 0.13 V and 0.12 V vs RHE, respectively, indicating alloying and nitridation-induced modification of the hydrogen adsorption properties and active surface sites. Linear sweep voltammetry (LSV) in H_2-saturated 0.1M KOH reveals the steady-state HOR performance (Figure 4b). All Ru based catalysts outperform Pt/C up to ~ 0.15 V vs RHE, delivering higher geometric current densities (j_{geo}) that highlight the intrinsic suitability of Ru surfaces for alkaline HOR (Figure S7). Among them, $RuNi_4N$-8515/C exhibits the most positive onset potential and the highest j_{geo} across the low overpotential region, surpassing $RuNi_4N$-7030/C, RuNi-8515/C, RuNi-7030/C, and Ru/C, consistent with its optimized composition and surface chemistry.

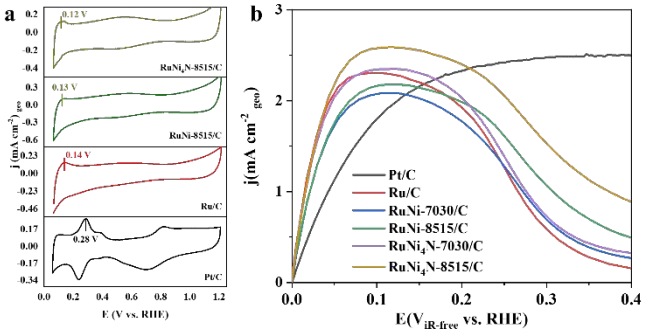

Figure 4. Electrochemical performance: a. CV curve of Pt/C, Ru/C, RuNi-8515/C and $RuNi_4N$-8515/C. b. LSV polarization curve of Pt/C, Ru/C RuNi-7030/C, RuNi-8515/C, $RuNi_4N$-7030/C and $RuNi_4N$-8515/C at 10 mV s^{-1}.

To quantitatively benchmark intrinsic HOR performance, specific activities ((ECSA-normalized) and mass activities were evaluated at 100 mV. ECSA values, obtained from copper underpotential deposition (Cu UPD) stripping voltammetry (Figure S8), show $RuNi_4N$-8515 at 108.2 $m^2\ g^{-1}$ and $RuNi_4N$-7030 at the highest value of 250 $m^2\ g^{-1}$ (Table S2). $RuNi_4N$-8515 exhibits the highest specific activity of 0.4 mA cm^{-2} and mass

activity of 156 A g_{Ru}^{-1} surpassing all counterparts: Ru/C (0.2 mA cm^{-2}, 112 A g^{-1}), RuNi-7030 (0.003 mA cm^{-2}, 125 A g^{-1}), RuNi-8515 (0.3 mA cm^{-2}, 131 A g^{-1}), and $RuNi_4N$-7030 (0.18 mA cm^{-2}, 147 A g^{-1}). Despite $RuNi_4N$-7030's superior ECSA (250 m^2 g^{-1} vs. 108 m^2 g^{-1} for $RuNi_4N$-8515), its lower specific activity reveals that surface abundance alone cannot account for the performance hierarchy, and that the optimal Ru: Ni ratio (85:15) combined with N-doping in $RuNi_4N$-8515 maximizes intrinsic activity per Ru site, over Ru/C.

This trend is consistent with the XPS/XAS evidence for electronic structural tuning of Ru-Ni centers. The progressive positive shift of the Ru 3p binding energy from Ru/C (462.3 eV) to $RuNi_4N$-8515 (462.8 eV) indicates electron withdrawal from Ru by both Ni (via electronegativity differences) and N-coordination, which weakens overly strong H* binding and brings the hydrogen binding energy closer to the optimum for HOR. EXAFS analysis confirms Ru-Ni coordination at ~2.36 Å, shorter than Ru-Ru in Ru foil, implying a contracted Ru environment, while the negative shift Ni 2p after nitridation suggests increased electron density at Ni sites, favoring OH* adsorption that accelerates the Volmer step in alkaline HOR. The combined effects tuned HBE on Ru, optimized OH binding on Ni/N sites, and a high density of accessible Ru-Ni ensembles lead to Pt-competitive HOR kinetics for $RuNi_4N$-8515/C and establish a clear structure-activity relationship for PGM-free alkaline HOR catalysts.

Previous DFT study on Ru-based HER catalysts[35] has shown that Ru is on the strong-H-binding side of the ΔG_H* volcano. Alloying with Ni[35] and support interactions with nitride downshifts the Ru d-band centre and brings ΔG_H* closer to the optimum. For alkaline HOR, optimized H* adsorption is also required to balance rapid H_2 dissociation with facile H* desorption, while suitable OH* binding on neighbouring oxyphilic sites is needed to accelerate the Volmer step. In $RuNi_4N$-8515/C catalyst, the positive shift of Ru 3p binding energy, the contracted Ru–Ni coordination from EXAFS and the H-UPD shift to lower potential correlate with the DFT-derived trend. These experimental signatures therefore provide indirect but compelling support for the conclusion that the enhanced HOR activity of $RuNi_4N$-8515/C arises from optimized adsorption/desorption behaviour at Ru–Ni–N interfacial sites, as beyond the alloying effect already reported.[36]

In conclusion, Pt free RuNi alloy and $RuNi_4N$/C catalysts deliver superior alkaline HOR performance through precise electronic and structural tuning. Nitriding optimizes Ru hydrogen binding energy while enhancing Ni mediated water dissociation, yielding marked gains in specific activity (0.4 mA cm^{-2}) and mass activity (156 A g^{-1}) at 0.1 V vs. RHE for $RuNi_4N$-8515. While the 85:15 Ru:Ni ratio maximizes intrinsic activity per site, 70: 30 compositions offer enhanced stability, revealing a composition-performance trade-off. XAFS confirms these effects arise from Ru-Ni coordination (2.36 Å) and N-modified electronic structure, establishing a clear structure-activity relationship for PGM-free HOR anodes.

Conflicts of interest

There are no conflicts to declare.

Data availability

All the data presented in an article is available in the manuscript.

Notes and references

1 P. P. Edwards, V. L. Kuznetsov, W. I. F. David and N. P. Brandon, *Energy Policy*, 2008, **36**, 4356–4362.

2 L. Zhang, C. Jia, F. Bai, W. Wang, S. An, K. Zhao, Z. Li, J. Li and H. Sun, *Fuel*, DOI:10.1016/j.fuel.2023.129455.

3 O. Lori and L. Elbaz, *ChemCatChem*, 2020, **12**, 3434–3446.

4 G. A. Goenaga, A. L. Roy, N. M. Cantillo, S. Foister and T. A. Zawodzinski, *J. Power Sources*, 2018, **395**, 148–157.

5 L. Zhao, H. Liu, Y. Liu, X. Han, J. Xu, W. Xing and W. Guo, *ACS Appl. Mater. Interfaces*, 2020, **12**, 40248–40260.

6 C. A. Campos-Roldán and N. Alonso-Vante, *Electrochem. Energy Rev.*, 2019, **2**, 312–331.

7 A. G. Oshchepkov, G. Braesch, A. Bonnefont, E. R. Savinova and M. Chatenet, *ACS Catal.*, 2020, **10**, 7043–7068.

8 Z. Zhou, Y. Liu, J. Zhang, H. Pang and G. Zhu, *Electrochem. commun.*, 2020, **121**, 106871.

9 S. Bulakhe, N. Shinde, J. S. Kim, R. S. Mane and R. Deokate, *Int. J. Energy Res.*, 2022, **46**, 17829–17847.

10 T. Wang, M. Wang, H. Yang, M. Xu, C. Zuo, K. Feng, M. Xie, J. Deng, J. Zhong, W. Zhou, T. Cheng and Y. Li, *Energy Environ. Sci.*, 2019, **12**, 3522–3529.

11 L. Su, D. Gong, N. Yao, Y. Li, Z. Li and W. Luo, *Adv. Funct. Mater.*, 2021, **31**, 1–8.

12 W. Ji, C. Zhan, D. Li, Y. Xu, Y. Zhang, L. Wang, L. Liu, Y. Wang, W. Chen, H. Geng and X. Huang, *J. Mater. Chem. A*, 2021, **9**, 26323–26329.

13 A. Munir, T. ul Haq, M. Saleem, A. Qurashi, S. Z. Hussain, F. Sher, A. Ul-Hamid, A. Jilani and I. Hussain, *Electrochim. Acta*, 2020, **341**, 136032.

14 H. Wang, Y. Yang, F. J. Disalvo and H. D. Abrunã, *ACS Catal.*, 2020, **10**, 4608–4616.

15 M. Alesker, I. Bakos, V. Davies, Q. Jia, L. Burlaka, V. Yarmiayev, A. Muzikansky, A. Kitayev, M. Page, S. Mukerjee and D. Zitoun, *Catal Sci Technol*, 2021, **11**, 1337–1344.

16 M. Shviro, S. Polani, R. E. Dunin-Borkowski and D. Zitoun, *Adv. Mater. Interfaces*, 2018, **5**, 1701666.

17 V. T. Veettil, M. Shanmugasundaram and D. Zitoun, *Energy Advances*, 2024, **3**, 2896–2902.

18 V. R. Stamenkovic, B. S. Mun, K. J. J. Mayrhofer, P. N. Ross and N. M. Markovic, *J. Am. Chem. Soc.*, 2006, **128**, 8813–8819.

19 C. Silva-Carrillo, E. A. Reynoso-Soto, J. R. Flores-Hernández, B. Trujillo-Navarrete, M. I. Salazar-Gastelum, T. R. Castañon, S. Perez-Sicairos, J. M. Romo-Herrera and R. M. Félix-Navarro, *Top. Catal.*, 2022, **65**, 1251–1261.

20 L. Wang, S. Meng, C. Tang, C. Zhan, S. Geng, K. Jiang, X. Huang and L. Bu, *ACS Nano*, 2023, **17**, 17779–17789.

21 C. A. Campos-Roldán, L. Calvillo, G. Granozzi and N. Alonso-Vante, *J. Electroanal. Chem.*, 2020, **857**, 113449.

22 L. An, X. Zhao, T. Zhao and D. Wang, *Energy Environ. Sci.*, 2021, **14**, 2620–2638.

View Article Online
DOI: 10.1039/D6CC01926A

23 Y. Zheng, Y. Jiao, Y. Zhu, L. H. Li, Y. Han, Y. Chen, M. Jaroniec and S. Z. Qiao, *J. Am. Chem. Soc.*, 2016, **138**, 16174–16181.

24 S. St. John, R. W. Atkinson, R. R. Unocic, T. A. Zawodzinski and A. B. Papandrew, *J. Phys. Chem. C*, 2015, **119**, 13481–13487.

25 J. Mahmood, F. Li, S. M. Jung, M. S. Okyay, I. Ahmad, S. J. Kim, N. Park, H. Y. Jeong and J. B. Baek, *Nat. Nanotechnol.*, 2017, **12**, 441–446.

26 Y. Li, J. Abbott, Y. Sun, J. Sun, Y. Du, X. Han, G. Wu and P. Xu, *Appl. Catal. B Environ.*, 2019, **258**, 117952.

27 X. Zhang, Z. Li, X. Sun, L. Wei, H. Niu, S. Chen, Q. Chen, C. Wang and F. Zheng, *ACS Mater. Lett.*, 2022, **4**, 2097–2105.

28 Y. Xue, L. Shi, X. Liu, J. Fang, X. Wang, B. P. Setzler, W. Zhu, Y. Yan and Z. Zhuang, *Nat. Commun.*, 2020, **11**, 1–8.

29 J. Mao, C. T. He, J. Pei, Y. Liu, J. Li, W. Chen, D. He, D. Wang and Y. Li, *Nano Lett.*, 2020, **20**, 3442–3448.

30 J. Liu, J. Wang, Y. Fo, B. Zhang, C. Molochas, J. Gao, W. Li, X. Cui, X. Zhou, L. Jiang and P. Tsiakaras, *Chem. Eng. J.*, 2023, **454**, 139959.

31 L. Han, P. Ou, W. Liu, X. Wang, H. T. Wang, R. Zhang, C. W. Pao, X. Liu, W. F. Pong, J. Song, Z. Zhuang, M. V. Mirkin, J. Luo and H. L. Xin, *Sci. Adv.*, 2022, **8**, 1–10.

32 L. Cai, W. Liu, Z. Cao, H. Li, Y. Cong, X. Zhu and W. Yang, *J. Memb. Sci.*, 2020, **599**, 117702.

33 E. S. Davydova, J. Zaffran, K. Dhaka, M. C. Toroker and D. R. Dekel, *Catalysts*, 2018, **8**, 1–19.

34 Z. Liang, H. Liu, S. Huang, M. Xing, Z. Li, S. Wang, L. Yang and D. Cao, *J. Mater. Chem. A*, 2022, **11**, 849–857.

35 L. Han, P. Ou, W. Liu, X. Wang, H.-T. Wang, R. Zhang, C.-W. Pao, X. Liu, W.-F. Pong, J. Song, Z. Zhuang, M. v Mirkin, J. Luo and H. L. Xin, *Sci. Adv.*, 2022, **8**, eabm3779.

36 X. Fu, Z. Chen, S. Zhang, J. Wang, J. Ding and X. Han, *Small*, **2024**, *20*, 2307725.

View Article Online
DOI: 10.1039/D6CC01926A

Data availability statement

All the data presented in an article is available in the manuscript.